ADVANCED MATERIALS
www.advmat.de

Uncovering the Network Modifier for Highly Disordered Amorphous Li-Garnet Glass-Ceramics

*Yuntong Zhu, Ellis R. Kennedy, Bengisu Yasar, Haemin Paik, Yaqian Zhang, Zachary D. Hood, Mary Scott, and Jennifer L.M. Rupp**

Highly disordered amorphous $Li_7La_3Zr_2O_{12}$ (aLLZO) is a promising class of electrolyte separators and protective layers for hybrid or all-solid-state batteries due to its grain-boundary-free nature and wide electrochemical stability window. Unlike low-entropy ionic glasses such as $Li_xPO_yN_z$ (LiPON), these medium-entropy non-Zachariasen aLLZO phases offer a higher number of stable structure arrangements over a wide range of tunable synthesis temperatures, providing the potential to tune the LBU-Li^+ transport relation. It is revealed that lanthanum is the active "network modifier" for this new class of highly disordered Li^+ conductors, whereas zirconium and lithium serve as "network formers". Specifically, within the solubility limit of La in aLLZO, increasing the La concentration can result in longer bond distances between the first nearest neighbors of Zr—O and La—O within the same local building unit (LBU) and the second nearest neighbors of Zr—La across two adjacent network-former and network-modifier LBUs, suggesting a more disordered medium- and long-range order structure in LLZO. These findings open new avenues for future designs of amorphous Li^+ electrolytes and the selection of network-modifier dopants. Moreover, the wide yet relatively low synthesis temperatures of these glass-ceramics make them attractive candidates for low-cost and more sustainable hybrid- or all-solid-state batteries for energy storage.

1. Introduction

Unraveling the potential of Li^+ batteries requires innovations in materials and cell design to meet the safety, manufacturing cost, and performance requirements for electric vehicles and emerging decarbonized technologies.[1–4] One of the most promising approaches is to replace the traditional organic liquid electrolytes with solid Li^+-ion-conducting electrolytes in an all- or semi-solid-state hybrid battery configuration and to pair these electrolytes with a Si/C or Li-metal anode for enhanced energy density, **Figure 1a**. In an all-solid-state battery design, the liquid electrolyte is fully substituted with a solid-state-electrolyte separator, requiring the electrolyte material to possess high Li^+ conductivity and excellent chemical and electrochemical stability with both the anode and cathode sides of the battery.[1] Alternatively, a hybrid battery design includes a thin Li^+-conducting protective coating layer toward the anode side, bridging the

Y. Zhu, H. Paik, Z. D. Hood, J. L. Rupp
Department of Materials Science and Engineering
Massachusetts Institute of Technology
Cambridge, MA 02139, USA
E-mail: jrupp@mit.edu

E. R. Kennedy, B. Yasar, Y. Zhang, M. Scott
Department of Materials Science and Engineering
University of California
Berkeley, CA 94720, USA

Z. D. Hood
Applied Materials Division
Argonne National Laboratory
9700 S. Cass Avenue, Lemont, IL 60439, USA

The ORCID identification number(s) for the author(s) of this article can be found under https://doi.org/10.1002/adma.202302438

DOI: 10.1002/adma.202302438

M. Scott
National Center for Electron Microscopy
Molecular Foundry
Lawrence Berkeley National Laboratory
Berkeley, CA 94720, USA

J. L. Rupp
Department of Chemistry
Technical University Munich
85748 Garching, Germany

J. L. Rupp
TUMint. Energy Research GmbH
Lichtenbergstr. 4, 85747 Garching, Germany

J. L. Rupp
Department of Electrical and Computer Engineering
Technical University Munich
80333 Munich, Germany

J. L. Rupp
Department of Electrical Engineering and Computer Science
Massachusetts Institute of Technology
Cambridge, MA 02139, USA

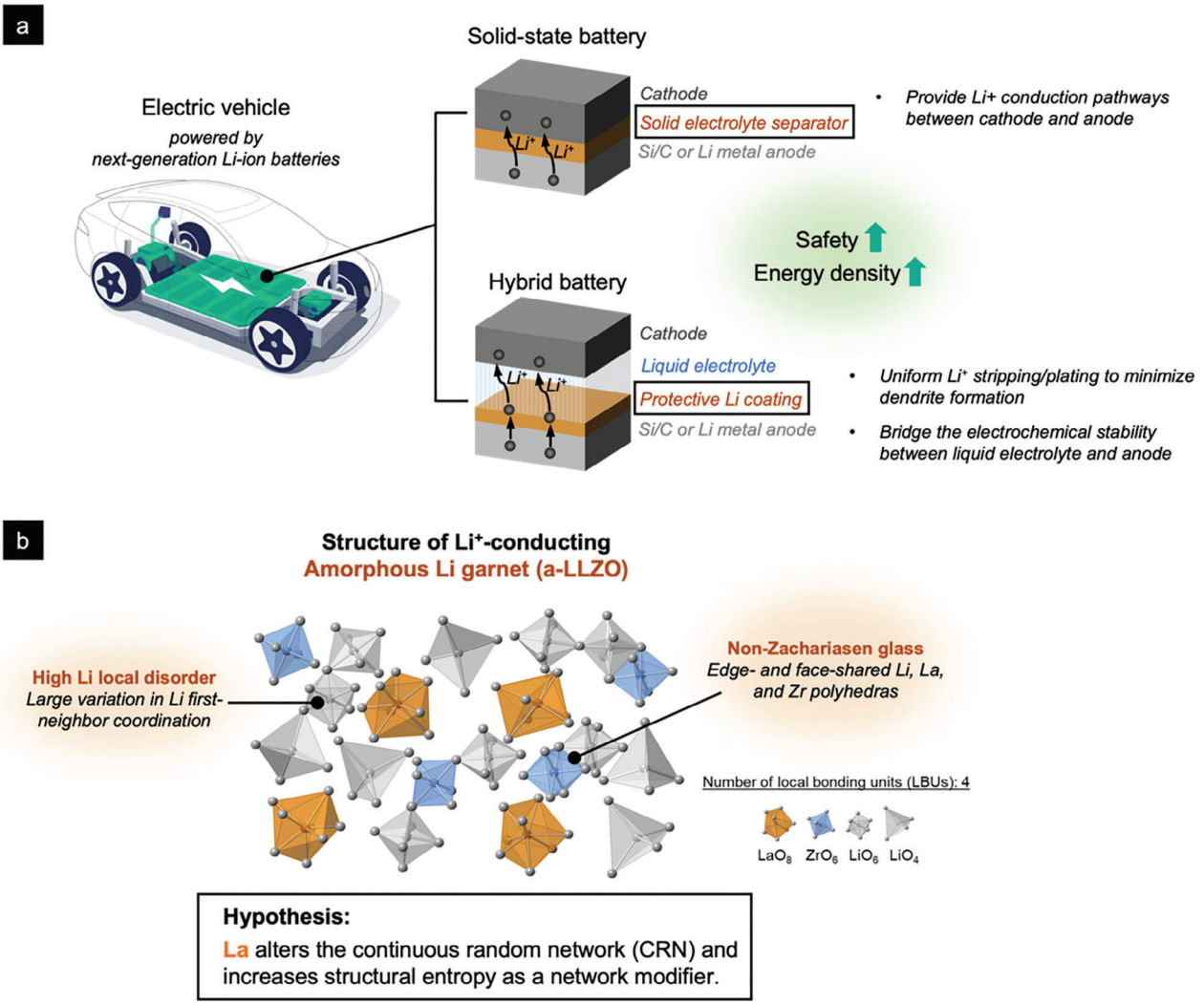

Figure 1. a) Schematic illustration of electric vehicles powered by next-generation Li^+ batteries, including a solid-state battery with a solid-electrolyte separator and a hybrid battery with a protective Li coating on the anode side. Both designs have the advantages of improved safety and energy density compared with state-of-the-art Li^+ batteries using organic liquid electrolytes. b) Structure of aLLZO based on four LBUs, that is, LiO_4, LiO_6, ZrO_6, and LaO_8.

electrochemical-stability voltage gap between the liquid electrolyte or sulfide-based electrolyte toward the Li anode and thus preventing interfacial reactions and Li-dendrite formation.[1,5] Solid-state electrolyte materials include oxide- and sulfide-based ceramics and glasses, which are attractive because of their enhanced resistance to Li-dendrite growth at high Li^+ conductivity[6] as well as the Li^+ transference number of nearly unity for certain oxide-based ones.[1] The sulfide-based electrolytes, such as argyrodite-type Li_6PS_5X (X = Cl, Br, I),[7,8] Li_2S—P_2S_5,[9,10] and $Li_{10}GeP_2S_{12}$ glasses,[11] have limited electrochemical stability windows (<1 V)[1,12,13] and have challenges for direct pairing with either a high-voltage cathode or Li anode. Thus, Li^+-conducting protective coatings are generally required for their applications in Li^+ batteries to widen the electrochemical stability window. In addition, sulfide-based electrolytes exhibit poor air stability, as they undergo a rapid hydrolysis reaction with moisture in the air and generate Li_2SO_4 and toxic H_2S gas,[14] which sets limits for their scalable production. The alternatives are oxide-based solid-state electrolytes such as garnet-type $Li_7La_3Zr_2O_{12}$ (LLZO),[15–17] which offer wider electrochemical stability windows[13] that can even enable direct pairing with Li anodes. Although oxide-based lithium phosphorous oxynitride glass $Li_xPO_yN_z$ (LiPON)[18–20] has by itself a limited electrochemical stability window that is unstable against Li, its formation of a thin and stable interphase layer composed of Li_3PO_4, Li_3N, Li_3P, and Li_2O at the anode–electrolyte interface[21–23] results in remarkable stability, that is, cells can operate for >10 000 stable cycles with the Li anode.[24]

Nonetheless, three major challenges remain in the battery integration of oxide-based solid-state electrolytes to achieve higher energy and power density and longer cycle life at reduced processing cost.

The first challenge concerns the "co-sintering of solid electrolytes and oxide-based cathodes". Oxide-based electrolytes often exhibit their best transport properties in crystalline phases,

requiring high-temperature sintering (e.g., >1050°C for cubic LLZO, cLLZO) to stabilize the desired highly conductive phase and achieve densification; see Refs. [1,3,16,25,26] for a more in-depth discussion. This high-temperature processing is not favorable for integration with the majority of Co-reduced and Co-free cathodes such as $LiNiMnCoO_2$ and $LiFePO_4$. The high temperatures required to solidify and stabilize the cathode–electrolyte solid interfaces lead to irreversible phase changes or decomposition of the cathode materials into low-capacity variants.[27,28] To ensure that the oxide-based cathode materials remain in their high-capacity phases with conventional solid electrolytes such as LLZO, unconventional manufacturing strategies are required to either shorten the sintering time by rapid thermal annealing, see Refs. [29–31] and therefore minimize the interfacial reaction, or maintain the co-processing temperature below 600 °C,[32] which is ≈400 °C lower than the classic co-sintering temperature, see Refs. [27,28] for details.

The second challenge is linked with the goal of "increasing critical current densities" for solid-state batteries to enhance their rate performance. It has been commonly observed that Li preferentially deposits along the grain boundary of a ceramic polycrystalline electrolyte.[6,33–35] One of the reasons is that the grain boundary is a sink of defects that often exhibits a lowered local Li^+ transference number (see evidence from electron microscopy[33–35] and opto-mechanical microscopy[6] experiments). The resulting local reduction and uneven deposition of Li can accelerate Li-dendrite growth and lead to battery failure at low critical current densities.[36] Alternative "grain-boundary-free" electrolyte concepts have been proposed as attractive options to mitigate dendrite growth at high current density.[37,38]

The third challenge is associated with "the high cost and energy consumption of solid-state battery manufacturing". An earlier cost analysis[3] indicates that the high-temperature annealing and sintering step is a major driver for the high processing costs in solid-state-battery manufacturing. In addition, the same- or higher-temperature processes are generally required for the end-of-life treatment for batteries, that is, pyrometallurgy recycling,[39] which add additional energy inputs and costs to the lifecycle of a battery and are unfavorable for environmental sustainability goals. This issue is exacerbated when energy costs rise, triggering a severe increase in production costs, as clearly exemplified in 2022, when the high cost of energy even led to the temporary closure of some glass and ceramic production lines in the United States. Hence, any opportunity for lowering the synthesis temperature of the Li^+-conducting electrolyte material (which is responsible for ≈75% of its cost) is significant for the market entry of solid-state batteries with further enhanced production sustainability.[3]

Low-temperature-processed Li^+ electrolyte films have been developed in the past years and applied in various solid-state and hybrid battery concepts. Amorphous oxide-based solid-electrolyte films offer good chemical and electrochemical stabilities against Li and do not require high-temperature sintering steps, attracting particular attention from the field. For instance, LiPON represents the most studied Li^+ electrolytes that are generally deposited using energy-intensive radio frequency sputtering. Its structure consists of only two types of local building units (LBUs) connected solely via corners (i.e., $P(O,N)_4$ and Li), and it can be classified as a non-Zachariasen ionic conducting invert glass.[40–42] Unlike the ionic glasses, aLLZO structures contain at least four unique LBUs, that is, LiO_4, LiO_6, ZrO_4, and LaO_8, and can be arranged in a greater variety of continuous random networks (CRNs) through a widened and processing-friendly temperature range (room temperature to 680 °C). These aLLZO phases contain edge- and face-shared LBUs, with Zr and Li being identified as "network formers" (which facilitate the formation of LBU connections via bridging oxygen) and the eightfold coordinated La considered a "network modifier" (which modulates the local disordering and therefore the Li^+ motion), Figure 1b.[40] Similar to the techno-historic evolution of the ionic glass conductor LiPON, the promising cell performance of the highly disordered aLLZO was first reported in all-solid-state thin-film batteries ahead of the understanding of its structure,[43] as summarized in **Figure 2** (see Supporting Information for more details). Without any structure optimization, the first aLLZO-based cell already exhibited excellent resistance against Li-dendrite formation up to 3.2 mA cm^{-2} (in contrast to the critical current density of 0.6–1 mA cm^{-2} generally observed for polycrystalline cLLZO).[43] To further improve the Li-transport dynamics and therefore the aLLZO-based cell performance, we consider modulating the near-order structure of aLLZO to be an attractive option. Specifically, the 8-coordinated La, among the 4 LBUs in aLLZO, does not form thermodynamically stable bonds with surrounding neighbors, and a small variation in its concentration and coordination can strongly affect the local order in aLLZO. However, studies on the effect of La on the aLLZO local structure and packing density remain lacking.

In the present study, we examine the hypothesis of whether La, as a network modifier in aLLZO, can be used to modulate the local structure of aLLZO. A combination of multiple spectroscopy, electron microscopy, and diffraction techniques are used to resolve the structural variation in medium-range order (MRO) and long-range order (LRO) upon changes in the La concentration. We confirm the role of La as a network modifier, identify its solubility limit, and discuss its effect on packing density and local chemistry. We consider this work relevant for the development of alternative network-modifier doping strategies in the aLLZO material class for further performance optimization as battery electrolytes or Li^+ protective coatings.

2. Results and Discussion

2.1. Role of La Concentration on the Phase Composition of Amorphous LLZO

In amorphous materials, the concentration of the network-modifier elements can generally affect the CRNs due to their thermodynamically metastable or unstable connections with the surrounding network-former LBUs. In this study, we test the hypothesis of whether the phase composition and local structure of aLLZO can be controlled by tuning the concentration of the network modifier, that is, eightfold-coordinated La. As such, we define as model structures and encompass a broad range of three La concentrations for the aLLZO ranging from 50 to 150 mol.%, that is, $Li_7La_{1.5}Zr_2O_{12-d}$ (low-La-concentration aLLZO), $Li_7La_3Zr_2O_{12-d}$ (medium-La-concentration aLLZO), and $Li_7La_{4.5}Zr_2O_{12-d}$ (high-La-concentration aLLZO). These

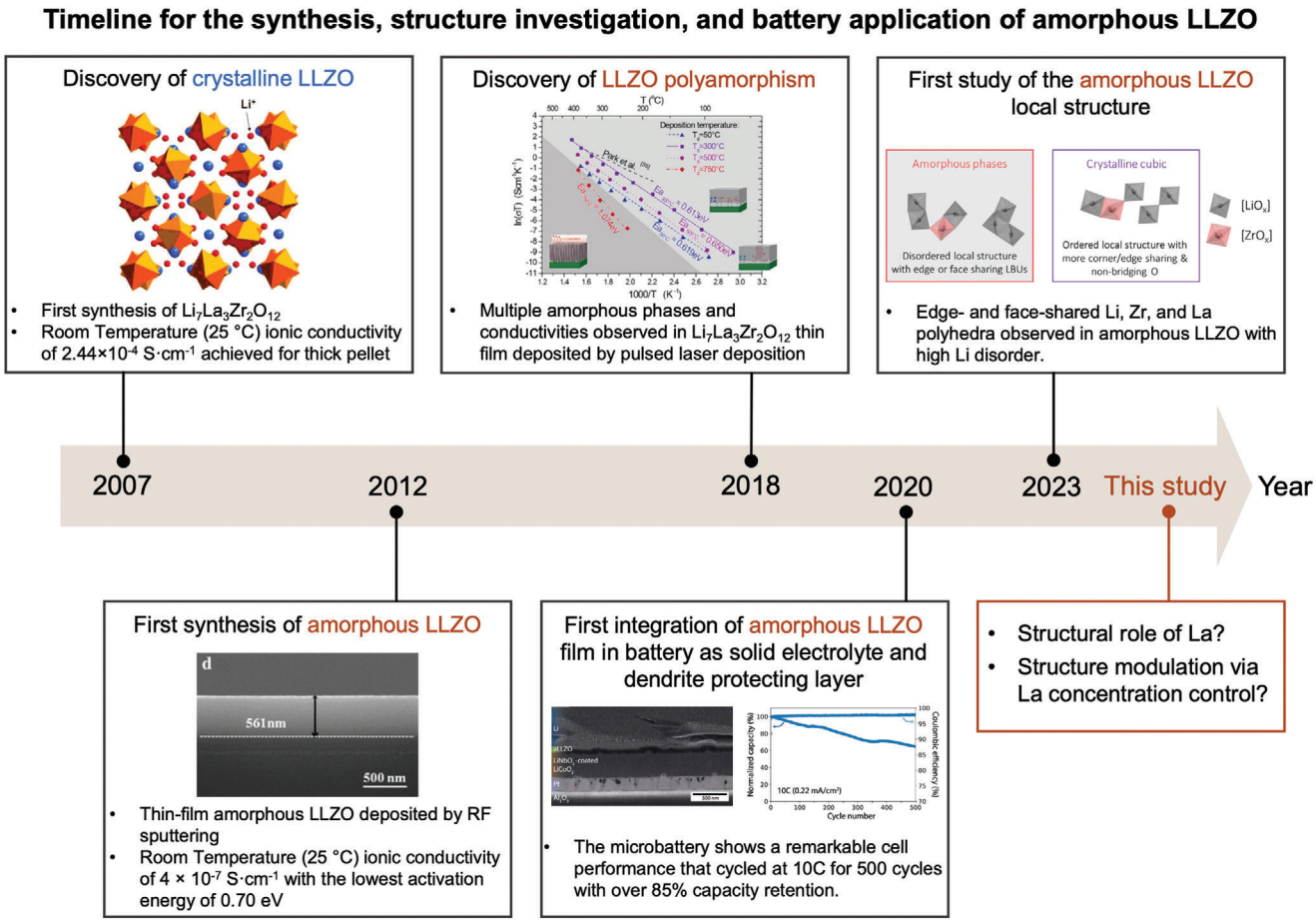

Figure 2. Timeline for the discovery of crystalline cubic LLZO (cLLZO) and the synthesis, structure investigation, and battery-cell application of aLLZO. Figure adapted with permission.[17,40,43,72,73].

model structures were synthesized via sequential decomposition synthesis (SDS)[44,45] at 300 °C, followed by post-annealing at 600 °C to fully decompose the precursor salts and attain aLLZO (see Figure S1, Supporting Information for more details). The surface and cross-sectional scanning electron microscopy (SEM) images of the post-annealed aLLZO films reveal a continuous and dense microstructure with film thicknesses of ≈1.1 ± 0.3 µm, **Figure** 3a. Increasing the La concentration in aLLZO leads to a higher film density and improved aLLZO surface smoothness, which can be attractive for application in solid-state or hybrid batteries to minimize interfacial resistance; the hypothesis of the role of La in aLLZO microstructure control can be found in Supporting Information, Figure S2 (Supporting Information). The in situ high-resolution transmission electron microscopy (HR-TEM) images in Figure 3b reveal the glass-ceramic nature of a medium-La-concentration aLLZO film, composed of a predominately amorphous Li-containing oxide phase and a minor phase of 4–8-nm isolated pyrochlore $La_2Zr_2O_7$ nuclei (see Fourier transform of HR-TEM image in Ref. [40]), depending on how long the film is post-annealed. At a longer annealing time, a larger fraction of the amorphous Li-containing oxide phase converts to isolated pyrochlore $La_2Zr_2O_7$ nuclei. This observation agrees with earlier reports on crystalline LLZO powder synthesis,[46,47] where $La_2Zr_2O_7$ (and in some routes, also La_2O_3)[46] was formed as an intermediate before Li incorporated into the structure.

Raman spectroscopy can be used to detect vibrational changes based on the local inelastic scattering of light and was therefore used to identify the local structure and phase composition of aLLZO films with La concentrations of 50, 100, and 150 mol.% (as compared to LLZO stoichiometry of $Li_7La_3Zr_2O_{12-d}$); the spectra are displayed in **Figure** 4a. We assigned vibrational modes to the observed Raman active peaks and performed a careful analysis on the O—Li—O and O—Zr—O peak shifts for the three aLLZO films with different La concentrations. As Li and Zr act as network formers in aLLZO (see analyses on Zr K-edge X-ray absorption spectroscopy (XAS) and ^{7}Li NMR in Ref. [40] for details), understanding their corresponding Raman shifts provides information on the effect of the La concentration on the CRN connection and packing density of aLLZO.

We first focus on the Raman spectra of the aLLZO films with low-to-medium La concentration, that is, 50 and 100 mol.% La. These spectra suggest a glass-ceramic nature of the films with peaks and uprising bands developing from aLLZO and minor crystalline phases of $La_2Zr_2O_7$ nuclei.

Specifically, in aLLZO phases with low-to-medium concentrations of La, we detected broad peaks centered at 410 and

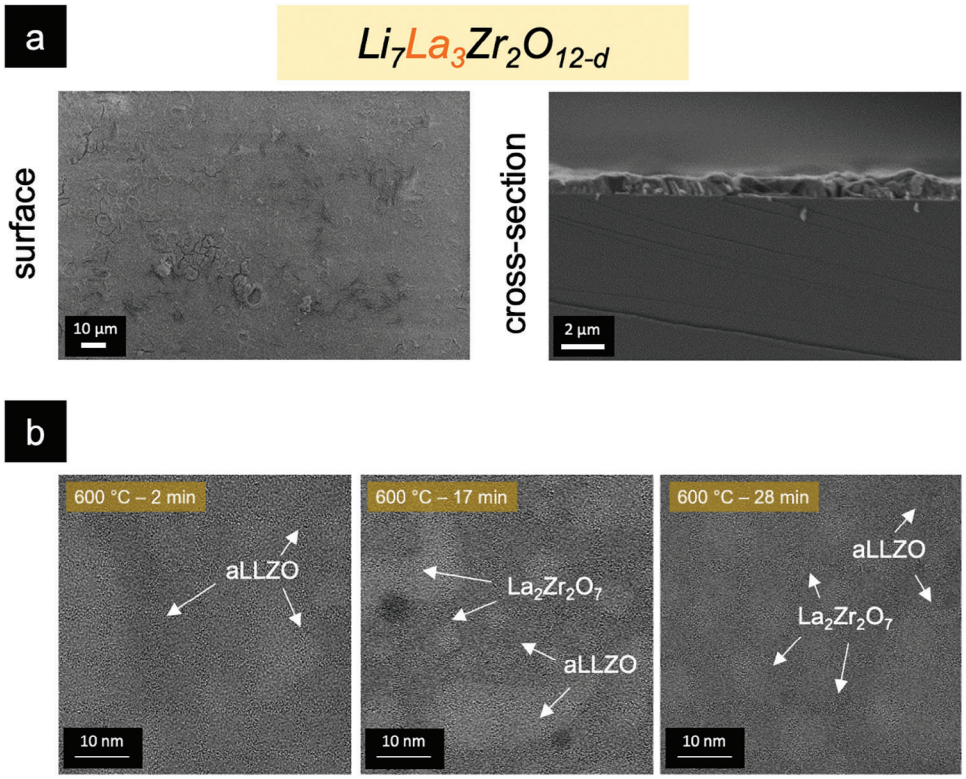

Figure 3. a) Surface and cross-sectional SEM images and b) HR-TEM image of 600 °C post-annealed aLLZO film with medium La concentration isothermally held for 2, 17, and 28 min. The film is composed of a predominately amorphous Li-containing oxide phase and isolated pyrochlore $La_2Zr_2O_7$ nuclei.

514 cm^{-1}, Figure 4b,c, and assigned them to the O—Li—O vibration bands (E_g and T_{2g}) in LiO_6 octahedra according to Ref. [49] Blueshifts of these E_g and T_{2g} peaks from 381 to 407 cm^{-1} and from 499 to 506 cm^{-1} occurred as the La concentration increased from low to medium concentration, suggesting, on average, a shorter Li—O bond distance in LiO_6 octahedra, Figure 4b,c. Furthermore, a broad uprising peak center at 651 cm^{-1} is attributed to the O—Zr—O stretching band (A_{1g} mode) in aLLZO;[48,49] Figure 4d provides a zoomed-in view of this A_{1g} Raman mode. In moving from low to medium La concentration, a pronounced redshift is observed for the O—Zr—O bond stretching from 588 to 578 cm^{-1}, signifying a longer Zr—O bond in the ZrO_6 octahedra. Moreover, an intense peak at 100 cm (T_{2g} mode) is attributable to O—La—O vibration in aLLZO.[48,49]

In addition to the Raman modes that correspond to the near-order vibrations from the amorphous phase, a prominent peak at ≈300 cm^{-1} was observed (attributed to the E_g mode of ZrO_6 bending),[50,51] suggesting the presence of minor $La_2Zr_2O_7$ nuclei in the glass-ceramic aLLZO. The Raman peak of the minor $La_2Zr_2O_7$ phase agrees with our previous study on aLLZO phase evolution during annealing, where $La_2Zr_2O_7$ nanocrystals formed as an intermediate phase during the crystallization of LLZO while the majority of the film remained amorphous (see Ref. [40] for further details). As displayed in Figure 4e, the E_g peak experienced a redshift from 292 to 302 cm^{-1} when increasing the La concentration from a low to medium level, suggesting, on average, a longer Zr—O bond in $La_2Zr_2O_7$ nuclei. We note that other lower-intensity Raman modes (i.e., F_{2g} and A_{1g} modes) of $La_2Zr_2O_7$ are not separable from the spectra, which may be merged or overshadowed by Raman modes of aLLZO and other minor phases.

Next, we turn to the Raman spectrum collected from the aLLZO film with a high La concentration, that is, 150 mol.% La. The spectrum suggests the phase composition of aLLZO with a high concentration of La differs significantly from that with a low-to-medium La concentration, as additional Raman modes appear in the high-La-concentration aLLZO spectrum and are assigned to the exsolution of La_2O_3 nuclei. Specifically, we observed prominent peaks at 110, 197, and 410 cm^{-1} in the spectrum of the high-La-concentration aLLZO film, corresponding to the E_g, A_{1g}, and E_g and A_{1g} modes of La—O stretching in and out of the (0 1 0) plane[52,53] in the hexagonal La_2O_3 structure, inset of Figure 4a. Similar phenomena were observed with La-site dopants, Ce^{4+}, and Li-site dopants, Fe^{3+}, in cLLZO, where nanocrystalline CeO_2 or $FeLaO_3$ precipitated out along the grain boundaries when Ce or Fe surpassed their solubility limit.[54,55] The rest of the Raman spectrum of the high-La-concentration aLLZO, however, does not allow the separation of vibrational modes that originate from the aLLZO phase. This observation may be explained by the highly disordered structure nature of aLLZO in high-La-concentration aLLZO that significantly increases the variation in Zr—O and Li—O bond distances, thus broadening the peaks; the broad and weak Raman modes may be overshadowed by the more pronounced Raman peaks from minor crystalline phases, such as La_2O_3 nuclei. In addition to the aforementioned glass-ceramic structures in the three different La-concentration

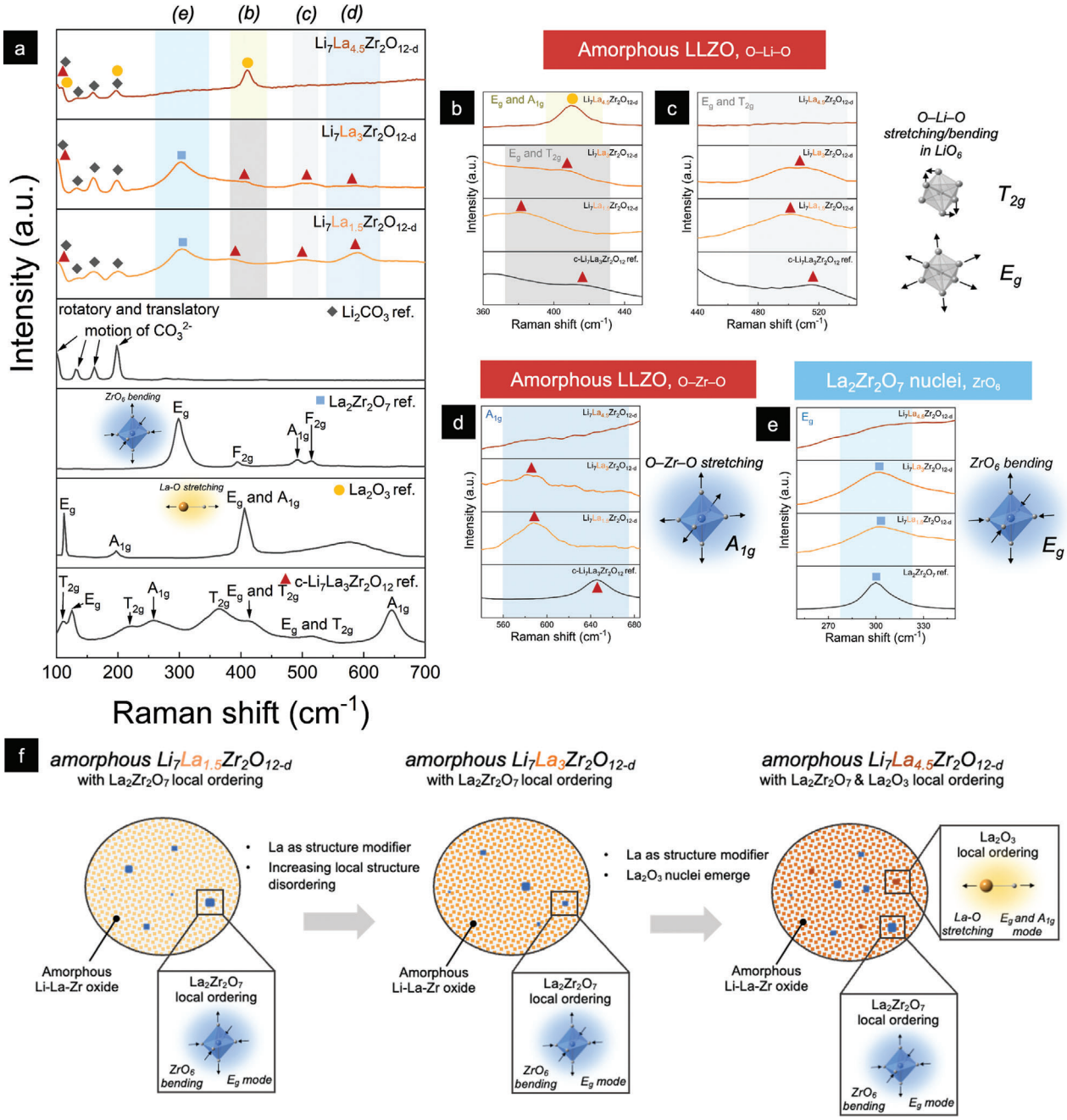

Figure 4. Effect of La concentration on the phase composition and near-order structure of aLLZO films. a) Raman spectra of aLLZO with low, medium, and high La concentrations. Additional reference spectra of Li_2CO_3, $La_2Zr_2O_7$, La_2O_3, and cubic $Li_7La_3Zr_2O_{12}$ are displayed in black. Insets: Graphic illustrations of E_g mode (300 cm^{-1}) of ZrO_6 bending in $La_2Zr_2O_7$ and of E_g and A_{1g} modes (406 cm^{-1}) of La—O stretching in La_2O_3. b,c) Zoom-in of Raman spectra in (a), emphasizing the O—Li—O vibration bands (E_g and T_{2g} modes) at b) ≈410 cm^{-1} and c) ≈514 cm^{-1} in LiO_6 octahedra. d,e) Zoom-in of Raman spectra in (a), emphasizing (d) the O—Zr—O stretching band (A_{1g} mode) of aLLZO and e) the ZrO_6 bending (E_g mode) of pyrochlore $La_2Zr_2O_7$ nuclei. f) Schematic illustration of the phase and local structure of aLLZO with low, medium, and high La concentrations based on the interpretation of the Raman spectra.

aLLZO films, minor peaks were also detected at 101, 132, 160, and 198 cm^{-1} in all three aLLZO spectra. These peaks are attributable to the rotatory and translator motion of CO_3^{2-} from the surface chemistry variation of Li_2CO_3,[56,57] which may originate from the direct contact of the films with moisture in the air[58,59] during sample transfer and spectroscopy measurements (see further details on the as-deposited aLLZO films in Figure S3, Supporting Information).

Collectively, based on the Raman spectra, we interpreted the role of the La concentration in the phase formation and composition of the aLLZO films, as presented in Figure 4f. We first confirmed the glass-ceramic nature of the aLLZO films,

composed in all cases of an amorphous LLZO phase with minor crystalline $La_2Zr_2O_7$ nuclei (and additional La_2O_3 nuclei in the high-La-concentration aLLZO). The aLLZO films with low-to-medium La concentrations, that is, $Li_7La_{1.5}Zr_2O_{12-d}$ to $Li_7La_3Zr_2O_{12-d}$, revealed that La acts as a network modifier in aLLZO; this is based on the observation that smaller Li—O bond distances and longer Zr—O bond distances prevail with increasing La concentration. These results serve as the first evidence that the bond lengths of the network modifiers Li and Zr with their first neighbor, O, can be successfully altered in these aLLZO structures via the network modifier, La. A prior study based on XAS suggests that longer Zr—O bonds in aLLZO are associated with more disordered and "jammed" local structures, where the network former, Zr LBU, exhibits a face-sharing tendency[40] with the network modifier, La LBU. Therefore, the medium-La-concentration aLLZO, that is, $Li_7La_3Zr_2O_{12-d}$, is suggested to consist of a more disordered amorphous local structure than the low-La-concentration one, that is, $Li_7La_{1.5}Zr_2O_{12-d}$. In addition, we detected a solubility limit of the La modifier that can be incorporated in an aLLZO structure with the threshold falling between 100 and 150 mol.% La in $Li_7La_3Zr_2O_{12-d}$.

It is challenging to probe the structure of amorphous metal oxides. One may conclude from this study that Raman spectroscopy provides useful insights for analyzing the near-order structure of aLLZO glass-ceramics; however, it is limited in its ability to describe atomic interactions beyond the first nearest neighbors. Thus, we turn to study the MRO structure of aLLZO through fluctuation electron microscopy (FEM) to gain further understanding of the effect of La-network-modifier modulations on the local packing density of aLLZO structures.

2.2. Medium-Range-Order Structure in Disordered Amorphous Regions of Amorphous LLZO

FEM is a scanning transmission electron microscopy (STEM) technique that measures the statistical fluctuations in the scattering of electrons arising from nanometer-scale ordered regions (generally in a length range of 0.5–2.0 nm)[60] and was therefore employed to characterize the effect of the La concentration on the MRO structure variations in the predominantly amorphous region of the aLLZO films (see Supporting Information for more details about FEM data collection and interpretation).

Figure 5a–c presents the normalized variance of the image intensity as a function of the scattering vector for the as-deposited and 600 °C in situ annealed aLLZO films with three different La concentrations, that is, 50 mol.% La, 100 mol.% La, and 150 mol.% La. The corresponding nanodiffraction images of the annealed aLLZO films are displayed as insets of Figure 5a–c. Our aim here is to investigate i) the local structure variation between as-deposited films and 600 °C annealed films, ii) the effect of the La concentration, varying from 50 to 150 mol.% La, on MRO formation. For aLLZO with all three La concentrations, two MRO peaks centered at scattering factors of 3.2 and 5.3 nm^{-1} (i.e., ≈3.1 and ≈1.9 Å, respectively) are identified and highlighted in gray and light orange in Figure 5a–c; these peaks correspond to the second and first nearest neighbor distances in aLLZO, respectively. The following characteristics are summarized from the FEM plots. First, the peak centered at 3.2 nm^{-1} appears in both the as-deposited and 600 °C annealed aLLZO, as opposed to the peak centered at 5.3 nm^{-1}, which was not observed in the as-deposited aLLZO with medium-to-high La concentrations. This observation suggests that the MRO at 5.3 nm^{-1} (1.9 Å) is not readily formed during SDS deposition but only upon annealing at 600 °C. Second, for each of these film compositions, the full width at half maximum (FWHM) of the peak centered at 3.2 nm^{-1} in the 600 °C annealed aLLZO film was smaller than that of the as-deposited film, suggesting the formation of more uniform second nearest neighbor distance with less disorder after the 600 °C annealing. This interpretation is corroborated by the Raman spectra collected from the as-deposited and annealed aLLZO, see Figure S3 (Supporting Information) and Figure 4a, where more prominent Raman bands and less local disorder were observed after 600 °C annealing for all three aLLZO compositions. Third, by comparing the intensity of the two peaks for each aLLZO composition, we identified that the relative intensity of the peak centered at 3.2 nm^{-1} to that of the peak centered at 5.3 nm^{-1} increases as the La concentration in aLLZO increases, suggesting that higher La concentration promotes the local order in aLLZO with a bond length of 3.1 Å.

We next performed Gaussian fitting for the two MRO peaks centered at 5.3 and 3.2 nm^{-1} to evaluate the effect of the La concentration on the MRO distances and their uniformity in the 600 °C annealed aLLZO. The fitted first nearest neighbor distance (peaks centered at 5.3 nm^{-1}) and second nearest neighbor distance (peaks centered at 3.2 nm^{-1}) are presented in Figure 5d, and their corresponding FWHM are summarized in Figure S4 (Supporting Information). First, as depicted in Figure 5d, both the first and second nearest neighbor distances show an initial increase for aLLZO with low to medium concentrations of La from 1.81 ± 0.01 to 1.98 ± 0.01 Å and from 3.08 ± 0.01 to 3.13 ± 0.01 Å, respectively. A moderate drop in the first and the second nearest neighbor distances to 1.92 ± 0.01 and 3.13 ± 0.01 Å follows for aLLZO with high La concentration, respectively. Second, the FWHM of the first MRO peak, Figure S4 (Supporting Information), exhibited a monotonic decreasing trend from 1.89 ± 0.08 to 1.77 ± 0.08 nm^{-1} for aLLZO with increasing La concentration from 50 to 150 mol.%, indicating more uniform bond lengths of ≈1.9 Å for higher-La-concentration aLLZO. Conversely, the FWHM of the second MRO peak, Figure S4 (Supporting Information), exhibited a monotonic increasing trend from 0.99 ± 0.03 to 1.17 ± 0.03 nm^{-1} for aLLZO films with higher La concentration, suggesting a wider distribution of the second nearest neighbor distance and the corresponding bond lengths ≈3.1 Å when increasing the La concentration in aLLZO.

To understand the effect of the MRO distances toward bonding, we compared the fitted peaks with literature data to identify the chemical bonds (and their bond distances) that correspond to the first and second nearest neighbor distances in aLLZO. We note that each MRO distance obtained from FEM measurements generally represents a group of bonds, and the Li-containing bonds are generally not detectable by FEM. To set the groundwork, we first summarized the local bonding distances of aLLZO[40] and crystalline cLLZO,[61] $Li_2Zr_2O_7$,[62] and La_2O_3[53] in Table S1 (Supporting Information) as these phases may exist in the 600 °C annealed aLLZO based on the Raman spectra in

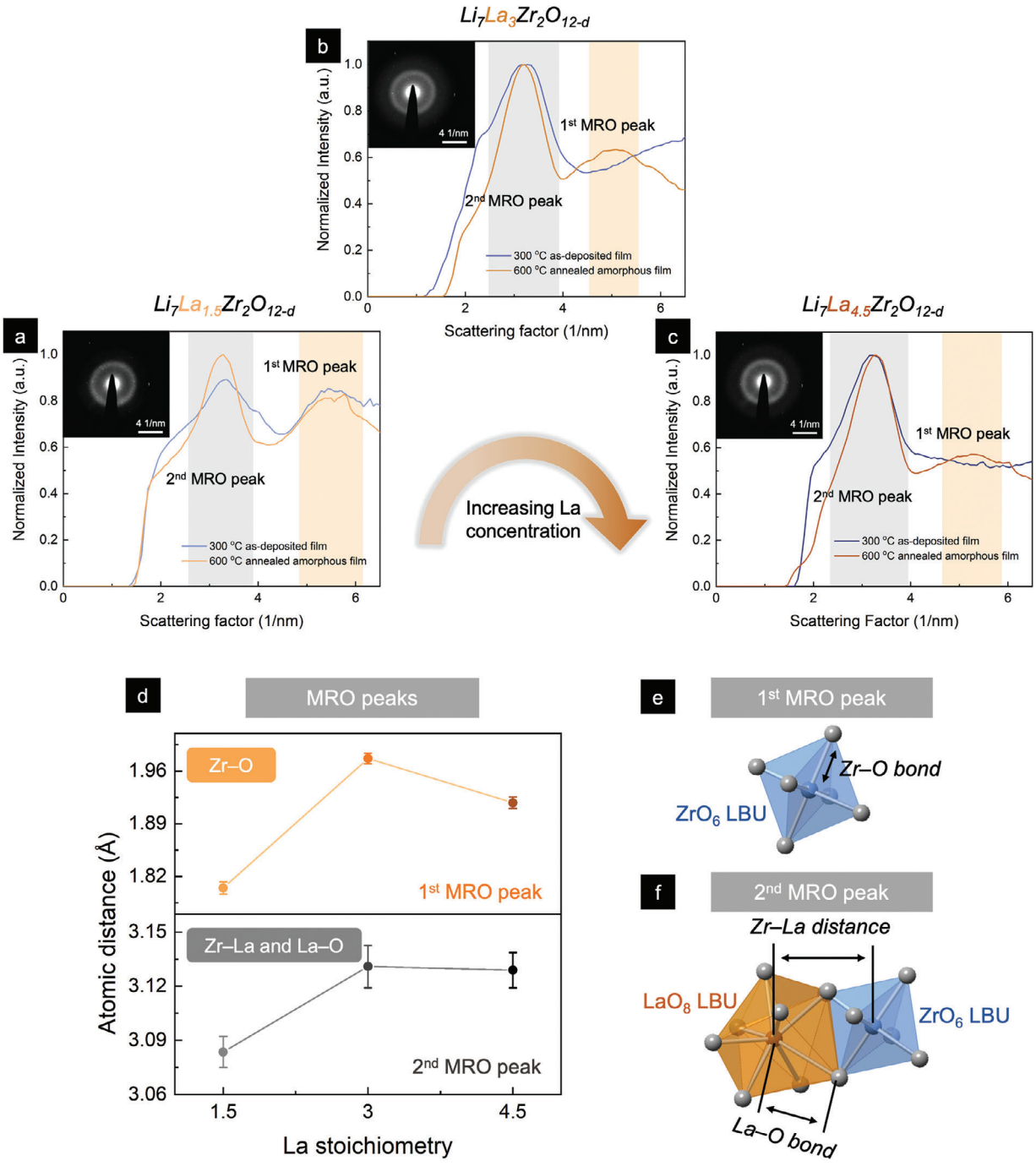

Figure 5. MRO measured by FEM applied to aLLZO with a) low, b) medium, and c) high La concentration. The peaks corresponding to the second and first MRO peaks are highlighted in light gray and light orange, respectively. d) first and second MRO peak positions as a function of the La content in aLLZO films. The first MRO peak is predominately attributable to the Zr—O bond. The second MRO peak is predominately attributable to Zr—La and La—O bonds. e) Structure of the ZrO_6 LBU in aLLZO. The Zr—O bond length matches most closely with the first MRO peak measured from FEM. f) Structure of the edge- or face-shared LaO_8 and ZrO_6 LBUs. The La—O and Zr—La distances match most closely with the second MRO peak measured from FEM. The ZrO_6 is presented as blue octahedra, and the LaO_8 is presented as yellow dodecahedra.

Figure 4a. Particularly, the nearest Zr—O bond was reported to have a bond length of 2.12 Å in aLLZO and cLLZO and 2.11 Å in $La_2Zr_2O_7$, suggesting that the first MRO peak observed in FEM (with a distance of ≈1.9 Å) could be correlated to the Zr—O bonds. In addition, the nearest La—O bond lengths and nearest Zr—La distances are also presented in Table S1 (Supporting Information), implying that the second MRO peak observed in FEM (with a distance of ≈3.1 Å) may be associated with both La—O and Zr—La distances. From a structure perspective, the Zr–O and La–O interactions indeed exist in aLLZO as the first nearest

neighbors to each other, forming direct bonds within the Zr and La LBUs, as displayed in Figure 5e, and the Zr–La interaction exists as the second nearest neighbors to each other, forming no direct bond, but rather as edge- or face-sharing LBUs,[40] as illustrated in Figure 5f.

Collectively, the role of the network modifier La and its effect on the MRO of aLLZO can be interpreted as consisting of two steps of structural evolution. First, for films with a low-to-medium La concentration, that is, $Li_7La_{1.5}Zr_2O_{12-d}$ to $Li_7La_3Zr_2O_{12-d}$, increasing the La concentration leads to further separation between both the first nearest neighboring Zr—O and La—O bonds within the LBUs and the second nearest neighboring Zr—La bond between the adjacent network-former and network-modifier LBUs. This finding corroborates the previous Raman spectra analysis, where we found that increasing La network-modifier concentrations promoted local structure disordering, as indicated by the red shifts of the O—Zr—O stretching band (A_{1g} mode) in Figure 4d. We note that the second MRO peaks are close to the Zr—La distances in edge- or face-shared LaO_8 and ZrO_6 LBUs for the probed aLLZO, not as edge-shared in a classic crystalline cLLZO. This finding agrees well with an independent XAS measurement, which previously indicated the face-sharing nature of La and Zr LBUs in aLLZO (see more information in Ref. [40]). Second, smaller MRO distances are detected for both the first and the second nearest neighbors upon further increasing the La concentration to 150 mol.% in aLLZO, which is possibly due to the presence of the exsolved La_2O_3 nuclei that promotes local-structure reordering, as detailed in the Raman section.

To obtain a full picture of the aLLZO phases and local structure upon variation of the La concentration, we next used grazing incident X-ray diffraction (GIXRD) to study the LRO in the nanocrystalline regions (i.e., $Li_2Zr_2O_7$ and La_2O_3).

2.3. Long-Range-Order Structure in Nanocrystalline La2Zr2O7 Nuclei

We consider it important to investigate these structure variations in the nanocrystalline regions of the films as different nuclei sizes and types could potentially alter the structure-reordering kinetics and, as a result, affect the packing density of aLLZO and potentially their Li^+ transport. Herein, we collected GIXRD patterns for the three aLLZO with different La concentrations to identify the crystalline phases within the nanocrystalline regions and their structure and grain-size variation, as displayed in **Figure 6a**. For all three aLLZO, crystalline peaks emerged at $\approx 2\theta = 28.5°$, 32.5°, 47.2°, and 56.8°, attributed to the (222), (400), (440), and (622) planes of the $La_2Zr_2O_7$ pyrochlore phase (*Fd-3m* space group), as illustrated in Figure 6c. The formation of crystalline LLZO can be excluded as no cLLZO or tetragonal LLZO (tLLZO) peaks were detected in the collected GIXRD patterns. In addition, peaks corresponding to Li_2CO_3 were also observed in the three aLLZO films, suggesting the variation in surface chemistry arising from the contact with moisture in the air, possibly during sample transfer and measurements. Interestingly, although the Raman spectra in Figure 4a imply the local ordering of La_2O_3 in the high-La-concentration aLLZO, La_2O_3 crystalline peaks were not detected in the corresponding XRD pattern. This observation presumably stems from the limited La_2O_3 nuclei sizes with less confined LRO structures, which, as a result, are not detectable by GIXRD. A peak at $2\theta = 42.5°$ appeared in all three aLLZO films, corresponding to the (200) plane of the single-crystal MgO substrates, depicted in Figure S5 (Supporting Information). Moreover, upon comparison to the GIXRD patterns of the as-deposited films in Figure S6 (Supporting Information), we noted that no crystalline phase was formed in the as-deposited films. Only a general amorphous background was observed with a broad hump centered at $2\theta = 28.5°$ for the three films, possibly corresponding to the nano-sized local ordering of $La_2Zr_2O_7$ with less confined bond distances. This result is consistent with previous studies on the LLZO phase evolution,[40] where the clear presence of $La_2Zr_2O_7$ nanocrystals only emerged and evolved upon post-annealing beyond 500 °C.

Significant shifts of the $La_2Zr_2O_7$ crystalline peaks are observed in the XRD patterns of the three aLLZO films in Figure 6a, generally indicating variation in the d-spacing within the crystalline nuclei. To better understand the effect of the La concentration on the structure and nuclei sizes of $La_2Zr_2O_7$, we performed peak fitting for the most prominent $La_2Zr_2O_7$ peak at $2\theta = 28.5°$ (the peak highlighted in red in Figure 6a), and the results are presented in Figure 6b. Specifically, the peak positions of $28.81 \pm 0.01°$, $28.32 \pm 0.01°$, and $28.82 \pm 0.01°$ in Figure 6b (more information can be found in Figure S7a, Supporting Information) and FWHMs of $1.07 \pm 0.01°$, $1.16 \pm 0.02°$, and $1.04 \pm 0.01°$ in Figure S7b (Supporting Information) were obtained from the XRD peak fitting for low-, medium-, and high-La-concentration aLLZO, respectively. From a structure perspective, the peak at $\approx 2\theta = 28.5°$ corresponds to the (222) plane in the $La_2Zr_2O_7$ pyrochlore structure, as presented in Figure 6c. The d-spacing between two (222) planes (denoted as the d_{222}-spacing in later discussion) can be interpreted as the distance between two planes consisting of ordered La and Zr atoms, as illustrated in Figure 6d.

Hence, we next applied Bragg's equation[63] and the Scherrer equation[64] to calculate the d_{222}-spacing and the average crystallite size of $La_2Zr_2O_7$ based on the peak position and FWHM data obtained from peak fitting. Figure 6e shows a volcano-shaped trend for the d_{222}-spacing, which increases from 3.10 ± 0.00 to 3.15 ± 0.00 Å in moving from the low- to medium-La-concentration aLLZO films and then decreasing to 3.10 ± 0.00 Å for the high-La-concentration aLLZO film. Conversely, the crystallite size (D) summarized in Figure 6f shows an initial drop from 7.68 ± 0.08 to 7.09 ± 0.09 nm in moving from the low- to medium-La-concentration aLLZO films, followed by an increase to 7.90 ± 0.08 nm for the high-La-concentration aLLZO film. The small errors in both the d_{222}-spacing and crystallite-size calculations indicate that the trends are significant.

Several important conclusions can be made from the GIXRD peak analysis. First, the calculated grain sizes of the $La_2Zr_2O_7$ nanocrystals in the three amorphous films fall within the range of <8 nm, similar to the observation in HR-TEM, displayed in Figure 3b, where $La_2Zr_2O_7$ with nuclei sizes of 4–8 nm is observed for the 600 °C aLLZO film. We hence confirmed that the films were predominately amorphous but exhibited a glass-ceramic nature with scattered $La_2Zr_2O_7$ nuclei. Second, for aLLZO with a low-to-medium La concentration, a larger d_{222}-spacing was observed for aLLZO with a higher La concentration; this result is in good agreement with the observed redshift of

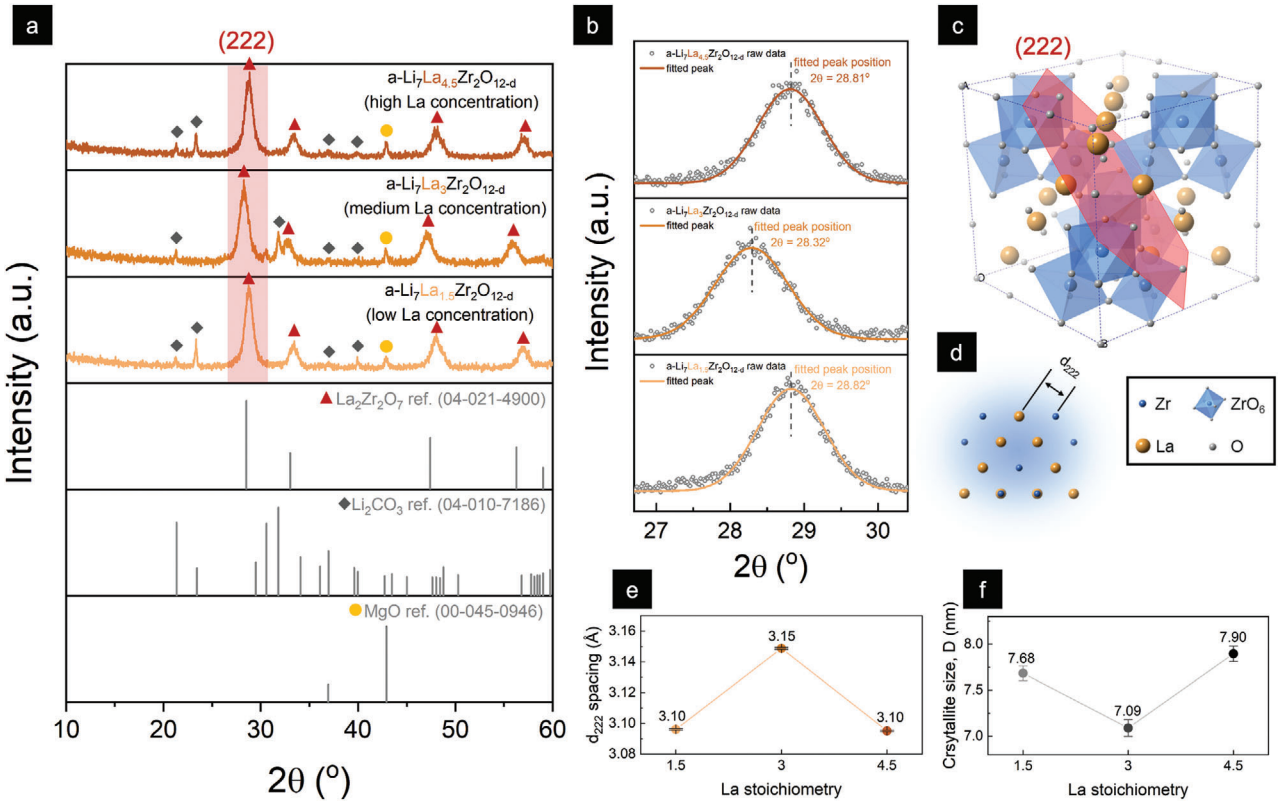

Figure 6. LRO structure for the crystalline regions in aLLZO. a) GIXRD patterns for aLLZO with low, medium, and high La concentrations. Broad peaks of $La_2Zr_2O_7$ and Li_2CO_3 were detected in all three aLLZO compositions. MgO peaks were detected from the substrates. References: $La_2Zr_2O_7$ (04-021-4900), Li_2CO_3 (04-010-7186), MgO (00-045-0946). b) Fitting of GIXRD peak in a 2θ range of 26.5–30.5° corresponding to the (222) plane of the pyrochlore $La_2Zr_2O_7$. The peak positions were fitted at 28.82°, 28.32°, and 28.81° for aLLZO with low, medium, and high La concentrations, respectively. c) Structure of pyrochlore $La_2Zr_2O_7$ (cubic, Fd-3m). The Zr, La, and O atoms are presented in blue, yellow, and dark gray, respectively, and the ZrO_6 is presented as blue octahedra. The (222) plane is highlighted in red. d) View of the d_{222} spacing of $La_2Zr_2O_7$ along the (110) direction. e) Calculated d_{222} spacing of $La_2Zr_2O_7$ as a function of La concentration in aLLZO. f) Calculated $La_2Zr_2O_7$ crystallite size (D) as a function of La concentration in aLLZO.

the E_g mode (ZrO_6 bending) in the Raman spectra, presented in Figure 4d, and is similar to the increased first and second MRO distances detected by FEM in Figure 5d. We relate this trend to the fact that La acts as a network modifier in aLLZO, promoting structure disorder and reducing the packing density in both amorphous and crystalline regions. Third, for films with a medium-to-high La concentration, increasing the La concentration leads to a larger $La_2Zr_2O_7$ nuclei size with reduced d_{222}-spacing. This feature can be attributed to the exsolution of heterogenous La_2O_3 nuclei, as suggested by Raman spectroscopy, which lowers the energy barrier for nucleation and growth within aLLZO glass-ceramics. Fourth, we observed that the calculated d_{222}-spacings (3.09–3.15 Å, the distances between two planes consisting of ordered La and Zr atoms in $La_2Zr_2O_7$ nuclei) are close to the second MRO distances (3.07–3.15 Å, mostly associated with La—O and Zr—La distances in aLLZO) obtained from FEM, as depicted in Figure 5d. We understand this observed concurrence in bond distances as the following. Part of the La and Zr LBUs in aLLZO that sit close to the already formed $La_2Zr_2O_7$ nuclei may arrange in an MRO with similar bond distances as in the $La_2Zr_2O_7$ nuclei, although the phase transition from aLLZO to $La_2Zr_2O_7$ is far from being completed and high local disorder in the LBU arrangement is still present and prevails. We present in the next section a summary of the role of La in the aLLZO structure and phase evolution with the MRO and LRO structure data collected from FEM and GIXRD and discuss their implications toward battery integration.

2.4. Modulating La Concentration in Amorphous LLZO toward Battery Applications

Figure 7 displays schematic illustrations of the phase and local structure of aLLZO with low-to-high La concentrations, that is, $Li_7La_{1.5}Zr_2O_{12-d}$, $Li_7La_3Zr_2O_{12-d}$, and $Li_7La_{4.5}Zr_2O_{12-d}$, based on the MRO and LRO structure analysis. First, we confirmed that aLLZO are generally composed of a predominate disordered amorphous phase with a minor presence of crystalline nuclei. On a microscopic level, we identify the role of La as a network modifier in aLLZO. When the La concentration is below its solubility limit in aLLZO (low-to-medium concentration of La), La fully dissolves in the amorphous structure matrix and promotes local structure disordering. Here, we observed looser LBU connections and larger MRO distances from Raman spectra and FEM analysis, as shown in Figure 4a and Figure 5d, as well as a larger d_{222}-spacing in crystalline $La_2Zr_2O_7$ regions with increasing La concentration up to

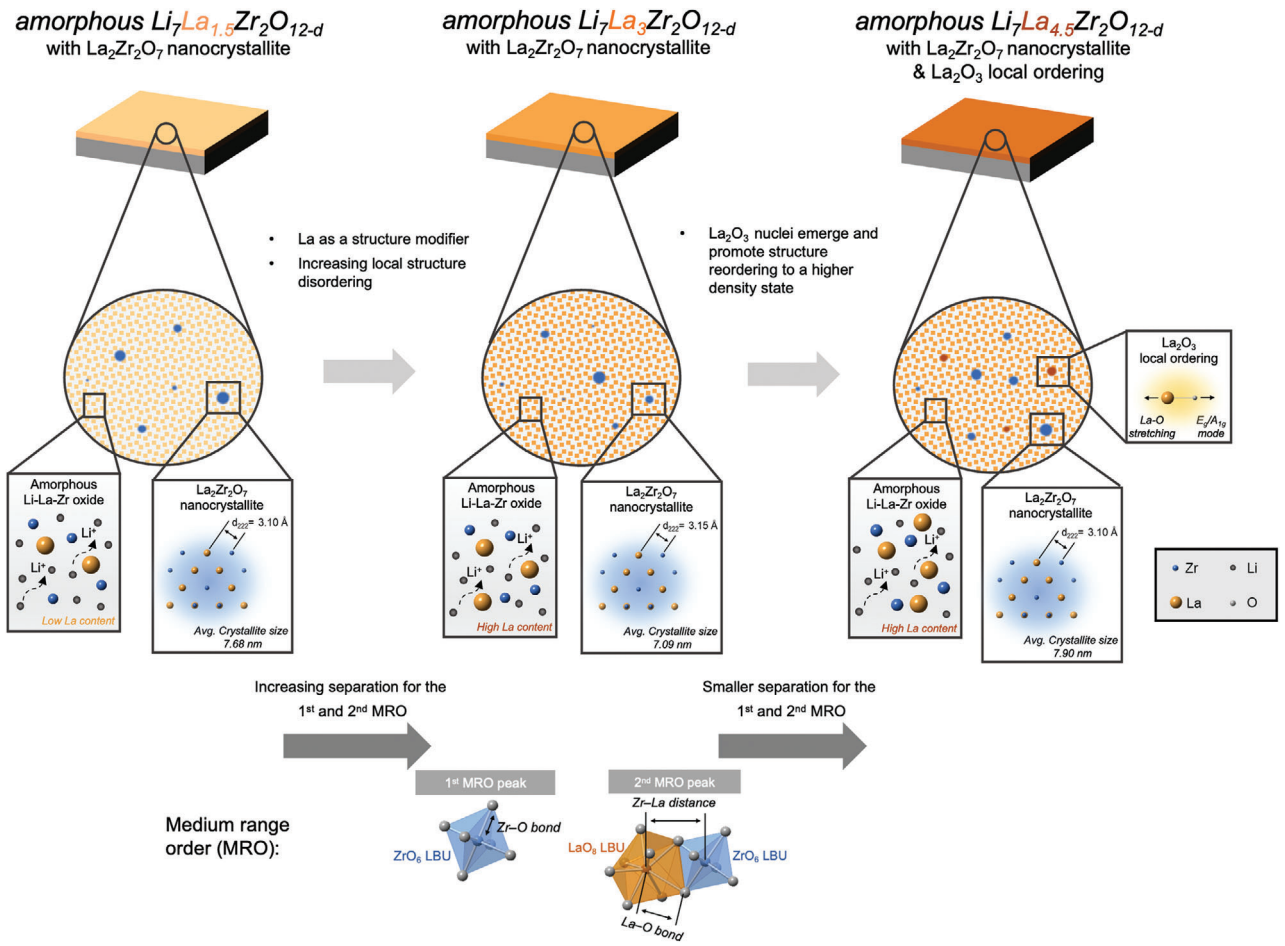

Figure 7. Schematic illustration of the phase and local structure of aLLZO with low, medium, and high La concentration, based on the interpretation of the collected Raman spectra, GIXRD patterns, and FEM diffraction data.

100 mol.% La, as displayed in Figure 6e. These observations suggest a lower packing density of aLLZO upon increasing the La concentration from a low to medium level. Once the La concentration exceeds its solubility limit in aLLZO, that is 150 mol.% La, the local ordering of La_2O_3 appears as secondary nanosized nuclei (detectable by Raman, but non-detectable by GIXRD) and promotes heterogenous nucleation with a lowered energy barrier for structure reordering. This leads to a more ordered and higher-packing-density local structure for aLLZO with a high La concentration. Specifically, larger nuclei sizes with smaller d_{222}-spacing nuclei are detected for crystalline $La_2Zr_2O_7$ nuclei and tighter LBU connections, and smaller first nearest neighbor distances are observed in the amorphous region of aLLZO. These findings showcase the role of the La network modifier in aLLZO and the solubility limit of La into various aLLZO phases, providing guidelines for future structure modulation.

Based on these findings, we see opportunities to modulate the local structure of aLLZO by doping various alternative network-modifier ions at the La sites. It was well known in the glass-ceramics field that not only the concentration of network-modifier elements but also the field strength (i.e., valence-to-radius ratio) can affect the coordination of the surrounding network-former LBUs, therefore altering the packing density and glass properties.[42,65] For instance, we are convinced that various to-be-explored La-site dopants can affect the coordination and packing density of the aLLZO glass-ceramics and significantly alter the Li^+ transport through the modulation of the Li^+ hopping pathway and distances. Future efforts can be focused on doping at La modifier sites with elements in the lanthanide series, for example, Ce and Er,[66] which have the same valence number and the same outermost-shell electronic structure but different atomic radii. Alternatively, one may consider group II elements, for example, Ca and Sr, as network-modifier dopants, which offer a "1+" difference in the valence state. Both strategies can alter the field strength surrounding the network-modifier elements and help achieve precise control over the coordination and connection of LBUs within aLLZO.

In terms of battery applications, the phase composition and glass packing density of aLLZO films are considered to be critical properties in determining their suitability for use as electrolyte separators or protective coating layers in cell designs, as they can affect the iontransport and mechanical properties of the aLLZO films, see detailed discussion on Li^+ transport properties of low-to-high La-concentration aLLZO film in Figure S8a,b (Supporting Information). Indeed, earlier studies on many other Zachariasen and non-Zachariasen invert glasses such as LiPON indicate that

the local bonding and electronic structure can be tuned by varying the type and concentration of network modifiers, and therefore, is a way to alter the transport properties of the glass.[42,67,68] We present here a model study that confirms the role of La in aLLZO as a network modifier, identifies the solubility limit of La in aLLZO, and provides effective ways to tune the packing density and phase composition of aLLZO films. Technologically, we see multiple opportunities for integrating the aLLZO films in solid-state or hybrid batteries, as illustrated in Figure 1a. They could be introduced as a Li protective coating layer between the Li-metal anode and liquid or sulfide electrolytes, reducing the tendency of Li-dendrite formation during Li plating and preventing the formation of a low-conduction SEI layer due to electrochemical instability at the interfaces. Alternatively, aLLZO films could be applied as a solid-electrolyte separator, providing Li^+ conduction while bridging the stability windows between the anode and cathode. Together with these efforts, we foresee the importance and applicability of our findings in guiding the design and optimization of aLLZO-based all-solid-state and hybrid batteries.

3. Conclusion

Amorphous Li^+ electrolyte films have been identified as promising candidates for use in all-solid-state or hybrid batteries as solid-electrolyte or protective-coating layers to further enhance the energy density and battery safety. Highly disordered Li-garnet-type aLLZO has attracted attention as an alternative to amorphous LiPON electrolytes owing to its wide electrochemical stability window, low vulnerability toward Li-dendrite growth (due to the elimination of highly dendrite-susceptible grain-boundary areas), and reduced yet wider thermal processing window (room temperature to 680 °C) to stabilize various amorphous phases.[3,40,69] In addition, aLLZO phases offer the opportunity to bypass the classic high-cost sintering processes typically required for crystalline Li^+-electrolyte synthesis, which becomes especially relevant with the recent spike in world energy prices. In 2023, medium-entropy aLLZO phases, composed of four different LBUs (namely, LiO_4, LiO_6, ZrO_6, and LaO_8) were described for the first time in terms of their LBU connections with their structure–Li^+ transport relations established, see Ref. [40] for details. Based on XAS and ^{7}Li NMR analyses, Li and Zr were clearly identified as network formers. However, it remained to be seen whether La was the effective network modifier in aLLZO and whether it could be used to modulate the MRO and LRO in aLLZO. Furthermore, the solubility limit of La in aLLZO solid solution remained unclear.

Through this study, we designed model cases of aLLZO structures, namely, $Li_7La_{1.5}Zr_2O_{12-d}$, $Li_7La_3Zr_2O_{12-d}$, and $Li_7La_{4.5}Zr_2O_{12-d}$, to probe the structural role of La and define its solubility limit in aLLZO. This study is crucial in determining potential dopant sites for network modifiers beyond La in aLLZO. Through near-order, MRO, and LRO structure probing techniques, we confirmed the glass-ceramic nature of the aLLZO films composed of a predominate amorphous phase and minor $La_2Zr_2O_7$ nuclei when La remains within its solubility limit in aLLZO. The MRO analysis via FEM confirmed, within the solubility of La, its role as a network modifier in aLLZO; increasing the La concentration leads to larger distances between the first nearest neighbors of Zr—O and La—O within the same LBU and the second nearest neighbors of Zr—La across two adjacent network-former and network-modifier LBUs. We also defined the solubility threshold between 100 and 150 mol.% for La in aLLZO via Raman spectroscopy. Through the definition of the role of La in aLLZO as a network modifier, we see perspective to explore in future work doping or co-doping strategies at La sites, including elements in the lanthanide series, alkaline-earth metals in group II, and high valance-state network modifiers identified in Zachariasen glass systems (e.g., Ga and Ta) for these medium-entropy aLLZO structures to further modulate structural and transport properties. We encourage both computational and experimental efforts to also investigate the optimum Li concentration on the tetragonal LiO_4 site and octahedral LiO_6 site and their impact on Li^+ site energies and diffusion mechanism.[70] Additional attention should be paid to the electrochemical stability between various aLLZO phases versus the Li-metal anode; it is also suggested that critical current densities be measured for various aLLZO phases designed based on careful selection of network-modulating dopants. Last but not least, the solubility limit of La in aLLZO could be further refined to reflect the precise threshold of structure modulation via tuning the concentration of La network modifier. Collectively, we are confident that with low-temperature and low-energy synthesis options to achieve manufacturing sustainability, amorphous Li garnets will be a material class of interest for future battery cell designs.

4. Experimental Section

Preparation of aLLZO Films by SDS: Three SDS precursor solutions were prepared in $Li_7La_{4.5}Zr_2O_{12-d}$, $Li_7La_3Zr_2O_{12-d}$, and $Li_7La_{1.5}Zr_2O_{12-d}$ stoichiometric ratio with 75% extra Li by dissolving $LiNO_3$, $La(NO_3)_3{\cdot}6H_2O$, and zirconium(IV) acetylacetonate into a solvent mixture of methanol:1-methoxy-2-propanol: bis(2-ethylhexyl) phthalate (1:1:1 vol.%). The concentration of the SDS solution was 0.015 M, and the solution was stirred overnight for 12 h before deposition. $LiNO_3$ (≥99%), zirconium(IV) acetylacetonate (97%), and 1-methoxy-2-propanol (≥99.5%) were purchased from Sigma-Aldrich; $La(NO_3)_3{\cdot}6H_2O$ (99.99%), and bis(2-ethylhexyl) phthalate were purchased from Alfa Aesar; methanol was purchased from VWR. Single-side-polished MgO (001) substrates (10 × 10 × 0.5 mm) were purchased from MTI Corporation and used as the substrate for SDS to prevent interfacial reactions.

The SDS of aLLZO starts with placing an MgO substrate on a heated stainless-steel hot plate at 300 °C with the polished side facing up. A K-type thermocouple was used to monitor the deposition temperature by placing it aside the MgO substrate. To deposit a film, the SDS solution was pumped through a polypropylene syringe at a rate of 10 mL h^{-1} into a spray atomizer (DeVILBLISS, AG361). Throughout the deposition, compressed gas with a pressure of 0.3 bar at the atomizer was selected as the carrier gas, and the distance between the spray atomizer and the MgO substrate was maintained at 25 cm. For each film stoichiometry, the as-deposited films were obtained after a 30-min deposition. To prepare the post-annealed aLLZO film, the as-deposited films were post-annealed in an alumina crucible in a temperature-calibrated tube furnace at 600 °C under a flow of pure O_2 (Airgas). A heating and cooling rate of 5 min $°C^{-1}$ was used to minimize surface strain on the films. The post-annealed aLLZO films were stored inside an Ar-filled glovebox before measurements to prevent exposure to moisture and minimize chemical degradation.

Microstructure Characterization: Surface and cross-sectional SEM images of the aLLZO films were collected using a Zeiss Ultra Plus field-emission scanning electron microscope with an accelerating voltage of 3.0–5.0 kV and a working distance of 3–8 mm. An in-lens secondary electron detector was used for SEM image collection in this study. A diamond blade was used to cut the sample before imaging the cross-section of the

films. Conductive carbon tape was used to tape the side of the samples to ensure sufficient electronic conductivity during imaging.

In Situ High-Resolution Transmission Electron Microscopy Characterization: HR-TEM was performed on an aberration-corrected FEI Titan S 8–300 TEM/STEM equipped with a Gatan Image Filter Quantum-865 operated at 300 kV. The specimen were prepared by depositing films via SDS (thicknesses of 50–80 nm) onto a MEMS-based heating chip (Protochips). A Protochips Aduro heating holder was used for the in situ heating experiments. The specimen were heated at a rate of 20 °C min^{-1} with isothermal dwells of 0.5–60 min to evaluate the atomistic evolutions during the post-processing of the films. The electron beam was carefully tuned to minimize any electron-beam-induced damage to the films. All TEM images and data were post-processed using DigitalMicrograph (Gatan Microscopy Suite) software.

Local Structure and Phase Composition Characterization: The near-order structure of aLLZO was characterized using Raman spectroscopy (WITec alpha 300 M+). A laser wavelength of 532 nm with a power of 10 mW, a grating of 300 g mm^{-1}, and a spectral resolution of 0.1 cm^{-1} were applied to obtain all the Raman data. A 50× long-distance objective (Zeiss, Germany) with a numerical aperture (NA) of 0.7 was used for the laser focusing, giving an approximate laser spot size of 1 µm.

MRO Structure Characterization: To prepare samples for in situ FEM measurements, the precursor solutions (0.015 M) were diluted to a concentration of 0.0003 M with methanol (VWR). The diluted solution was cast onto a silicon TEM grid (Norcada, TA301Z). Each grid contained a 3 × 3 array of 0.1 × 0.1 mm windows covered by 10-nm-thick silicon nitride membranes.

A FEI heating holder was used for the in situ experiments. The samples were heated at 300 and 600 °C, respectively, on the TitanX, operated at 200 keV. At each temperature, FEM patterns were collected with a convergence angle of 0.51 mrad, a probe diameter of 2.2 nm, and a camera length of 245 mm. For each sample, over 400 scanning nanodiffraction images were collected in one scan. As FEM was a statistical approach, to reduce the error in FEM analysis, four scans for each sample were collected. For FEM data analysis, a custom MATLAB script was used to calibrate the data by removing the ellipticity and to determine the differences in variance as a function of the spatial frequency as a function of the scattering angle. Data processing and analysis were performed, following the procedure outlined in Ref. [71] Two decimal places and a 95% confidence interval were reported for the atomic distances and FWHM obtained from the fitted MRO peaks.

LRO Structure Characterization: GIXRD patterns of both the as-deposited and post-annealed aLLZO films were collected using a Rigaku SmartLab diffractometer with Cu Kα irradiation (λ = 1.5406 Å). An omega angle of 1°, a scan step size of 0.02° at a speed of 5° per minute, an X-ray voltage of 45 kV, and a current of 200 mA over the 2θ angular range of 15°–60° were used for all the measurements. Automatic *z*-axis height adjustment was applied based on the intensity of the XRD signal. The XRD patterns were used for peak fitting to obtain the changes in the peak position and FWHM for the annealed samples. Note that the peak positions of the annealed samples were not corrected by the refractive index as the films were mostly amorphous with undefined refractive index. This could potentially lead to a maximum of 0.1° of error in the peak position due to minor differences in the sample alignment during the XRD measurements, which would not change the trend depicted from the current peak fitting. Bragg's equation, $n\lambda = 2d\sin\theta$, was used to calculate the d-spacing of the $La_2Zr_2O_7$ nanocrystals, where n is an integer (n = 1 is used for this study), λ is the X-ray wavelength (1.5406 Å), d is the spacing of the diffracting planes, and θ is the Bragg angle. The crystallite domain sizes (D) were obtained using Scherrer's equation, $D = K\lambda/(\beta\cos\theta)$, where K is the dimensionless shape factor (K = 0.9 used for this study), λ is the X-ray wavelength (1.5406 Å), β is the FWHM in radians, and θ is the Bragg angle.

Supporting Information

Supporting Information is available from the Wiley Online Library or from the author.

Acknowledgements

Y.Z. acknowledges financial support from the MIT Energy Initiative fellowship offered by ExxonMobil. J.L.M.R. thanks the Thomas Lord Foundation for financial support. This work made use of the MRSEC Shared Experimental Facilities at MIT, supported by the National Science Foundation under award number DMR-1419807. This work was performed in part at the Center for Nanoscale Systems (CNS), a member of the National Nanotechnology Coordinated Infrastructure Network (NNCI), supported by the National Science Foundation under NSF award no. 1541959. CNS was part of Harvard University. The transmission electron microscopy analysis was performed at the Molecular Foundry at Lawrence Berkeley National Laboratory. Work at the Molecular Foundry was supported by the Office of Science, Office of Basic Energy Sciences, of the U.S. Department of Energy under Contract No. DE-AC02-05CH11231. A portion of the electron microscopy research was conducted as part of a user project at the Center for Nanophase Materials Sciences (CNMS), which is a US Department of Energy, Office of Science User Facility at Oak Ridge National Laboratory.

Conflict of Interest

The authors declare no conflict of interest.

Author Contributions

Y.Z. and J.L.M.R. proposed the model of the study. Y.Z., E.R.K., B.Y., H.P., Y.Z., and Z.D.H. designed and performed the experiments. All the co-authors contributed to the discussion and data analysis. Y.Z. wrote the manuscript with the help of all the co-authors.

Data Availability Statement

The data that support the findings of this study are available from the corresponding author upon reasonable request.

Keywords

amorphous oxides, Li7La3Zr2O12, Li garnets, Li-conducting glass-ceramics, solid-state batteries

Received: March 16, 2023
Revised: January 24, 2024
Published online:

[1] K. J. Kim, M. Balaish, M. Wadaguchi, L. Kong, J. L. M. Rupp, *Adv. Energy Mater.* **2021**, *11*, 2002689.
[2] K. J. Kim, J. J. Hinricher, J. L. M. Rupp, *Nat. Energy* **2020**, *5*, 278.
[3] M. Balaish, J. C. Gonzalez-Rosillo, K. J. Kim, Y. Zhu, Z. D. Hood, J. L. M. Rupp, *Nat. Energy* **2021**, *6*, 227.
[4] C. Bauer, S. Burkhardt, N. P. Dasgupta, L. A.-W. Ellingsen, L. L. Gaines, H. Hao, R. Hischier, L. Hu, Y. Huang, J. Janek, C. Liang, H. Li, J. Li, Y. Li, Y.-C. Lu, W. Luo, L. F. Nazar, E. A. Olivetti, J. F. Peters, J. L. M. Rupp, M. Weil, J. F. Whitacre, S. Xu, *Nat. Sustainability* **2022**, *5*, 176.
[5] K. K. Fu, Y. Gong, G. T. Hitz, D. W. McOwen, Y. Li, S. Xu, Y. Wen, L. Zhang, C. Wang, G. Pastel, J. Dai, B. Liu, H. Xie, Y. Yao, E. D. Wachsman, L. Hu, *Energy Environ. Sci.* **2017**, *10*, 1568.
[6] J. H. Cho, K. Kim, S. Chakravarthy, X. Xiao, J. L. M. Rupp, B. W. Sheldon, *Adv. Energy Mater.* **2022**, *12*, 2200369 .

[7] H. J. Deiseroth, S.-T. Kong, H. Eckert, J. Wannahme, C. Reiner, T. Zaiss, M. Schlosser, *Angew. Chem., Int. Ed.* **2008**, *47*, 755.
[8] S. Boulineau, M. Courty, J. M. Tarascon, V. Viallet, *Solid State Ionics* **2012**, *221*, 1.
[9] F. Mizuno, A. Hayashi, K. Tadanaga, M. Tatsumisago, *Adv. Mater.* **2005**, *17*, 918.
[10] X. Yu, et al., *J. Electrochem. Soc.* **1997**, *144*, 524.
[11] L. Schweiger, K. Hogrefe, B. Gadermaier, J. L. M. Rupp, H. M. R. Wilkening, *J. Am. Chem. Soc.* **2022**, *144*, 9597.
[12] H. Xu, Y. Yu, Z. Wang, G. Shao, *Energy Environ. Mater.* **2019**, *2*, 234.
[13] Y. Zhu, X. He, Y. Mo, *J. Mater. Chem. A Mater.* **2016**, *4*, 3253.
[14] H. Muramatsu, A. Hayashi, T. Ohtomo, S. Hama, M. Tatsumisago, *Solid State Ionics* **2011**, *182*, 116.
[15] Q. Liu, Z. Geng, C. Han, Y. Fu, S. Li, Y.-B. He, F. Kang, B. Li, *J. Power Sources* **2018**, *389*, 120.
[16] S. Afyon, F. Krumeich, J. L. M. Rupp, *J. Mater. Chem. A Mater.* **2015**, *3*, 18636.
[17] R. Murugan, V. Thangadurai, W. Weppner, *Angew. Chem., Int. Ed.* **2007**, *46*, 7778.
[18] J. B. Bates, N. J. Dudney, G. R. Gruzalski, R. A. Zuhr, A. Choudhury, C. F. Luck, J. D. Robertson, *J. Power Sources* **1993**, *43*, 103.
[19] J. B. Bates, N. J. Dudney, B. Neudecker, A. Ueda, C. D. Evans, *Solid State Ionics* **2000**, *135*, 33.
[20] Y. Zhu, X. He, Y. Mo, *ACS Appl. Mater. Interfaces* **2015**, *7*, 23685.
[21] A. Schwobel, R. Hausbrand, W. Jaegermann, *Solid State Ionics* **2015**, *273*, 51.
[22] D. Cheng, T. A. Wynn, X. Wang, S. Wang, M. Zhang, R. Shimizu, S. Bai, H. Nguyen, C. Fang, M.-C. Kim, W. Li, B. Lu, S. J. Kim, Y. S. Meng, *Joule* **2020**, *4*, 2484.
[23] Z. D. Hood, X. Chen, R. L. Sacci, X. Liu, G. M. Veith, Y. Mo, J. Niu, N. J. Dudney, M. Chi, *Nano Lett.* **2021**, *21*, 151.
[24] J. Li, C. Ma, M. Chi, C. Liang, N. J. Dudney, *Adv. Energy Mater.* **2015**, *5*, 1401408.
[25] R. Mahbub, K. Huang, Z. Jensen, Z. D. Hood, J. L. M. Rupp, E. A. Olivetti, *Electrochem. Commun.* **2020**, *121*, 106860.
[26] J. Lin, L. Wu, Z. Huang, X. Xu, J. Liu, *J. Energy Chem.* **2020**, *40*, 132.
[27] L. Miara, A. Windmüller, C.-L. Tsai, W. D. Richards, Q. Ma, S. Uhlenbruck, O. Guillon, G. Ceder, *ACS Appl. Mater. Interfaces* **2016**, *8*, 26842.
[28] K. J. Kim, J. L. M. Rupp, *Energy Environ. Sci.* **2020**, *13*, 4930.
[29] C. Wang, W. Ping, Q. Bai, H. Cui, R. Hensleigh, R. Wang, A. H. Brozena, Z. Xu, J. Dai, Y. Pei, C. Zheng, G. Pastel, J. Gao, X. Wang, H. Wang, J.-C. Zhao, B. Yang, X. R. Zheng, J. Luo, Y. Mo, B. Dunn, L. Hu, *Science* **1979**, *368*, 521.
[30] X. Tao, L. Yang, J. Liu, Z. Zang, P. Zeng, C. Zou, L. Yi, X. Chen, X. Liu, X. Wang, *J. Alloys Compd.* **2023**, *937*, 168380.
[31] T. Clemenceau, N. Andriamady, M. K. P. Kumar, A. Badran, V. Avila, K. Dahl, M. Hopkins, X. Vendrell, D. Marshall, R. Raj, *Scr. Mater.* **2019**, *172*, 1.
[32] Y. Zhu, M. Chon, C. V. Thompson, J. L. M. Rupp, *Angew. Chem., Int. Ed.* **2023**, *62*, e2023045.
[33] F. Han, A. S. Westover, J. Yue, X. Fan, F. Wang, M. Chi, C. Wang, *Nat. Energy* **2019**, *4*, 187.
[34] E. J. Cheng, A. Sharafi, J. Sakamoto, *Electrochim. Acta* **2017**, *223*, 85.
[35] X. Liu, R. Garcia-Mendez, A. R. Lupini, Y. Cheng, Z. D. Hood, F. Han, A. Sharafi, J. C. Idrobo, N. J. Dudney, C. Wang, C. Ma, J. Sakamoto, M. Chi, *Nat. Mater.* **2021**, *20*, 1485.
[36] M. Golozar, A. Paolella, H. Demers, S. Savoie, G. Girard, N. Delaporte, R. Gauvin, A. Guerfi, H. Lorrmann, K. Zaghib, *Sci. Rep.* **2020**, *10*, 18410.
[37] M. B. Dixit, B. S. Vishugopi, W. Zaman, P. Kenesei, J.-S. Park, J. Almer, P. P. Mukherjee, K. B. Hatzell, *Nat. Mater.* **2022**, *21*, 1298.
[38] Y. Zhu, M. Balaish, J. L. M. Rupp, *Joule* **2022**, *6*, 2680.
[39] Y. Huang, J. Li, *Adv. Energy Mater.* **2022**, *12*, 2202197.
[40] Y. Zhu, Z. D. Hood, H. Paik, P. B. Groszewicz, S. P. Emge, F. N. Sayed, C. Sun, M. Balaish, D. Ehre, L. J. Miara, A. I. Frenkel, I. Lubomirsky, C. P. Grey, J. L. M. Rupp, *Matter* **2024**.
[41] V. Lacivita, N. Artrith, G. Ceder, *Chem. Mater.* **2018**, *30*, 7077.
[42] C. Calahoo, L. Wondraczek, *J. Non-Cryst. Solids: X* **2020**, *8*, 100054.
[43] J. Sastre, M. H. Futscher, L. Pompizi, A. Aribia, A. Priebe, J. Overbeck, M. Stiefel, A. N. Tiwari, Y. E. Romanyuk, *Commun. Mater.* **2021**, *2*, 76.
[44] Z. D. Hood, Y. Zhu, L. J. Miara, W. S. Chang, P. Simons, J. L. M. Rupp, *Energy Environ. Sci.* **2022**, *15*, 2927.
[45] Y. Zhu, Z. D. Hood, J. L. M. Rupp, L. J. Miara (USA), 11757127, **2022**.
[46] R. L. Sacci, R. D. McAuliffe, T. F. Malkowski, N. Kidder, X. C. Chen, A. Huq, M. Kirkham, B. L. Armstrong, L. L. Daemen, G. M. Veith, *Inorg. Chem.* **2021**, *60*, 10012.
[47] A. Paolella, W. Zhu, G. Bertoni, S. Savoie, Z. Feng, H. Demers, V. Gariepy, G. Girard, E. Rivard, N. Delaporte, A. Guerfi, H. Lorrmann, C. George, K. Zaghib, *ACS Appl. Energy Mater.* **2020**, *3*, 3415.
[48] F. Tietz, T. Wegener, M. T. Gerhards, M. Giarola, G. Mariotto, *Solid State Ionics* **2013**, *230*, 77.
[49] G. Larraz, A. Orera, M. L. Sanjuán, *J. Mater. Chem. A Mater.* **2013**, *1*, 11419.
[50] B. P. Mandal, P. S. R. Krishna, A. K. Tyagi, *J. Solid State Chem.* **2010**, *183*, 41.
[51] B. E. Scheetz, W. B. White, *J. Am. Ceram. Soc.* **1979**, *62*, 468.
[52] J. Gouteron, D. Michel, A. M. Lejus, J. Zarembowitch, *J. Solid State Chem.* **1981**, *38*, 288.
[53] A. Orera, G. Larraz, M. L. Sanjuán, *J. Eur. Ceram. Soc.* **2013**, *33*, 2103.
[54] E. Rangasamy, J. Wolfenstine, J. Allen, J. Sakamoto, *J. Power Sources* **2013**, *230*, 261.
[55] D. Rettenwander, C. A. Geiger, M. Tribus, P. Tropper, R. Wagner, G. Tippelt, W. Lottermoser, G. Amthauer, *J. Solid State Chem.* **2015**, *230*, 266.
[56] M. H. Brooker, J. Wang, *Spectrochim. Acta, Part A* **1992**, *48*, 999.
[57] Y. Hase, I. V. P. Yoshida, *Monatsh. Chem.* **1980**, *111*, 1265.
[58] Y. Arinicheva, X. Guo, M.-T. Gerhards, F. Tietz, D. Fattakhova-Rohlfing, M. Finsterbusch, A. Navrotsky, O. Guillon, *Chem. Mater.* **2022**, *34*, 1473.
[59] H. Huo, J. Luo, V. Thangadurai, X. Guo, C.-W. Nan, X. Sun, *ACS Energy Lett.* **2020**, *5*, 252.
[60] P. M. Voyles, D. A. Muller, *Ultramicroscopy* **2002**, *93*, 147.
[61] Y. Chen, E. Rangasamy, C. Liang, K. An, *Chem. Mater.* **2015**, *27*, 5491.
[62] A. A. Yastrebtsev, V. V. Popov, A. P. Menushenkov, A. I. Beskrovnyi, D. S. Neov, I. V. Shchetinin, K. V. Ponkratov, *J. Alloys Compd.* **2020**, *832*, 154863.
[63] R. A. Millikan, C. Structure, *Science* **1914**, *40*, 174.
[64] P. Scherrer, *Nachr. Ges. Wiss. Goettingen, Math.-Phys. Kl.* **1918**, *2*, 98.
[65] T. Oey, K. F. Frederiksen, N. Mascaraque, R. Youngman, M. Balonis, M. M. Smedskjaer, M. Bauchy, G. Sant, *J. Non Cryst. Solids* **2019**, *505*, 279.
[66] J. C. Slater, *J. Chem. Phys.* **1964**, *41*, 3199.
[67] O. L. Anderson, D. A. Stuart, *J. Am. Ceram. Soc.* **1954**, *37*, 573.
[68] L. Murawski, *J. Mater. Sci.* **1982**, *17*, 2155.
[69] Y. Zhu, J. C. Gonzalez-Rosillo, M. Balaish, Z. D. Hood, K. J. Kim, J. L. M. Rupp, *Nat. Rev. Mater.* **2021**, *6*, 313.
[70] S. Wang, Y. Liu, Y. Mo, *Angew. Chem., Int. Ed.* **2023**, *62*, e202215544.
[71] E. Kennedy, N. Reynolds, L. Rangel DaCosta, F. Hellman, C. Ophus, M. C. Scott, *Appl. Phys. Lett.* **2020**, *117*, 091903.
[72] D. J. Kalita, S. H. Lee, K. S. Lee, D. H. Ko, Y. S. Yoon, *Solid State Ionics* **2012**, *229*, 14.
[73] I. Garbayo, M. Struzik, W. J. Bowman, R. Pfenninger, E. Stilp, J. L. M. Rupp, *Adv. Energy Mater.* **2018**, *8*, 1702265.